

Introduction

Fluidized bed spray granulation is a process in which particle growth is induced through the injection of solids in liquid form into a granulator, either as a melt, or suspended or dissolved in a liquid. The process is illustrated in Fig. 1.1. Here, a particle bed is fluidized using the inflowing air and thereby mixed. Droplets are injected through a nozzle and deposited on the particles. After deposition, the liquid interacts with the gas phase. In the case of melt granulation, the gas acts as a cooling agent and forces the solids to solidify whereas in the case of solution or suspension granulation, the liquid evaporates. In this work, the focus is laid on the treatment of solutions or suspension rather than melt granulation.

Fluidized bed spray granulation is commonly chosen for its consistency in producing products with sharply defined properties or functionality. It is thus widely used in the food industry, pharmaceutical industry as well as consumer product and chemical industries. These resulting product properties are the consequence of the local conditions that particles experience over the course of the process. Local process conditions include the deposition of spray droplets onto the particle surface, contact with other particles and evaporation of liquid on the surface, as well as heat transfer with the gas phase. The fluidization gas introduces agitation into the system and allows for evaporation of the liquid. The physics

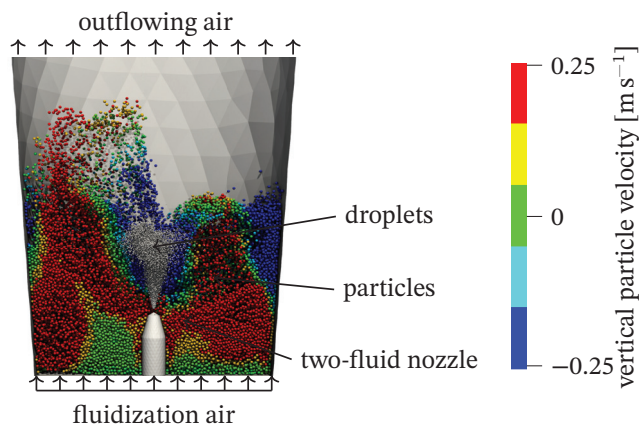


Fig. 1.1.: Snapshot of a CFD-DEM simulation of the particle and droplet dynamics inside a Glatt GF3 granulator in operation, with particles clipped away up to the mid-plane.

of fluidization allow for excellent heat and mass transfer due the intense interaction of these two phases.

Depending on the properties and amount of spray liquid applied and the velocities at which particles collide, they may either grow in layers due to the solids contained in the liquid, or by particles agglomerating together. Layer growth occurs for high velocity impacts, spray liquids with a low surface tension and viscosity, and low spray rates (equating to low local liquid concentrations). Here, contacts of wetted particles will not lead to sticking. This is both because wetted contacts rare occur, and the contacts endure for durations that are too short to result in solidification or sintering (Salman et al., 2006).

Hoffmann et al. (2015) and Diez et al. (2018) identified the global drying potential

$$\eta = \frac{Y_{in}^{wb} - Y_{out}}{Y_{in}^{wb} - Y_{in}} \quad (1.1)$$

to correlate with a wide range of layering granulation product properties such as porosity, yield strength and surface roughness when spraying a solution of a salt. Y is the specific humidity loading and Y_{in}^{wb} the wet-bulb humidity that would occur in the granulator if the enthalpy of the inflowing air is used for evaporation until the saturation point is reached. Values approaching $\eta = 1$ indicate low spray rates or high inflowing gas temperatures because the energy budget of the inflowing air is large compared to rate at which liquid is evaporated. In contrast, values close to $\eta = 0$ indicate low gas temperatures and high spray rates, indicating that the outflowing air already reached its saturation point and no further evaporation can occur. The drying potential is an indirect descriptor for the rate at which the droplets and wetted particles dry in the granulator, showing that these are key factors in granulation. However, correlating the drying potential with product properties fails when spraying suspensions (Schmidt et al., 2017b). Another important branch of layering spray granulation is the use of melts, for which no quantitative morphology studies could be found in literature at the time of this work.

The other process, agglomeration, occurs when the spray liquid and process conditions are tailored to let particle collisions lead to sticking and solidification. Particular focus is laid on the strength of liquid bridges between two colliding particles. The stability of the process is dependent on an equilibrium between solid bridges forming and breaking. When bridges, that are much stronger than the stresses in the system, form, unbounded agglomerate growth occurs, causing fluidization to cease. On the other hand, bridges that are weaker than the stresses in the system would break, leading to the prior case of layer growth.

Fluidization, the key phenomenon at the heart of fluidized bed granulation, can nowadays

be accurately described with numerical methods, most notably and suitably the coupled Computational Fluid Dynamics-Discrete Element Method (CFD-DEM), as described by Tsuji et al. (1992). The trajectories of up to tens of millions of individual particles (or parcels) can be resolved with limited effort and their exchange of heat and mass with the gas phase can be tracked. Despite that, fully space-resolved simulations where the structure of particles themselves is resolved still pose a substantial challenge. Therefore, a variety of indirect approaches have been developed to use simulation technologies.

Terrazas-Velarde et al. (2009) used a Monte Carlo approach to describe agglomeration in fluidized bed spray granulation by tracking discrete, stochastic events. Based on this, Dadkhah et al. (2012) were able to accurately model agglomerate structure. The weakness of Monte Carlo approaches lie in the need to provide probabilities for events and other closures, such as for the collision velocity of particles. Some works, such as those of Dosta et al. (2013), have developed elaborate ways to bridge length- and time scales by deriving closures from CFD-DEM simulations. Kafui and Thornton (2008) directly described agglomerate growth using CFD-DEM simulations with cohesion / surface-energy modelling, albeit for a very small system. Fries et al. (2014) used the CFD-DEM method to investigate the resulting properties of fluidized bed spray agglomeration. They were successful in predicting agglomerate breakage strength by using the aforementioned growth-breakage equilibrium for a variety of different granulator geometries without having to rely on a wide variety of closures.

Few studies have been performed with respect to product properties of fluidized bed layering spray granulation. Hoffmann (2016) used experimental closures based on the global drying potential to describe the growth of particles using a population balance model. For the surface structures formed by layering granulation, Jiang et al. (2020) performed CFD-DEM simulations coupled to a Monte Carlo method with discretized particle surfaces to characterize the inter-particle homogeneity of layer formation, albeit with no correlation to the actual particle porosity.

1.1. Aim of this Work

The aim of this work is the maturation of simulation technology for performing predictive simulations of the fluidized bed spray granulation process at any given apparatus scale. To this end, two focus points were chosen:

- Simulation of weakly wetted granular matter.
- Prediction of fluidized bed spray layering granulation product properties.

Both aims are independent of each other for the purpose of this thesis. The ability to model the influence of liquid distribution on dynamics allows to determine whether agglomeration or layering granulation will take place. Finding a calibration approach to describe weakly wetted, sensitive systems is therefore one of the aims of this thesis.

The other focus is the development and application of an approach for the prediction of fluidized bed spray layering granulation using CFD-DEM simulations, leveraging knowledge of the conditions under which drying occurs. To this end, an approach is to be developed that

- works for spray liquids that are solutions or suspensions and
- can predict deviations in product properties that occur in scale-up.

This is to be done in a manner that is easy and reproducible.

1.2. Structure of this Work

Chapter 2 gives an overview of the classical Discrete Element Method and Computational Fluid Dynamics techniques and their coupling. This provides the theoretical foundation that is later built upon.

The succeeding content chapters are split into two parts. The first part addresses the aim of describing weakly wetted granular systems. In chapter 3, an overview of the physics involved in liquid bridges is given, a model is composed and a new liquid bridge state model is proposed. The sensitivities of characterization experiments with respect to the liquid bridge model parameters are analyzed and a calibration workflow is proposed on the basis of these specific sensitivities. The approach is applied to a real material system in chapter 4.

For the second part, a product-property prediction approach for fluidized bed layering spray granulation is devised in chapter 6. The applicability of this approach to the use of suspensions as the spray liquid is shown in chapter 7 and the applicability to using salt solutions as the spray liquid is shown in chapter 8. This is done by demonstrating the ability to find a mapping between the conditions that particles experience and the product property chosen. Chapter 9 then applies the mapping derived in chapter 8 to a pilot-scale case and demonstrates the predictiveness of the approach in scale-up by a factor of 8.

Numerical Simulation of Particulate Flows using CFD-DEM

The CFD-DEM (Computational Fluid Dynamics-Discrete Element Method) is a versatile, deterministic method of simulating fluid-solid flows due to its ability to represent both the gaseous flow and the solid particles in their most natural frames of reference respectively. An expansive overview of the range of applications it is used for can be found in Kieckhefen et al. (2020), from which this chapter was derived.

In this chapter, a short description of the individual DEM and CFD methods are given, followed by an overview of the details that must be considered when coupling these methods.

2.1. Governing Equations of the Discrete Element Method

In the Discrete Element Method (DEM), as proposed by Cundall and Strack (1979), particle motion is resolved by numerically integrating the Newtonian equations of motion:

$$\ddot{\mathbf{x}}_i = \frac{1}{M_i} \left(\sum_j \mathbf{F}_{j \rightarrow i} + \mathbf{F}_{i,\text{ext}} \right) \quad (2.1)$$

$$\dot{\boldsymbol{\omega}}_i = \frac{1}{J_i} \left(\sum_j \mathbf{T}_{j \rightarrow i} + T_{i,\text{ext}} \right) \quad (2.2)$$

where \mathbf{x}_i is the position of a particle i , M_i refers to its mass and $\mathbf{F}_{i,\text{ext}}$ to the external forces acting upon it, such as inter-phase drag and gravity. $\boldsymbol{\omega}_i$ is the angular momentum, J_i the moment of inertia and $\mathbf{T}_{j \rightarrow i}$ the torque acting on i due to j . The inter-particle contact force $\mathbf{F}_{j \rightarrow i} = \mathbf{F}_{j \rightarrow i}^n + \mathbf{F}_{j \rightarrow i}^t$ of particle j acting upon particle i are composed of a normal component $\mathbf{F}_{j \rightarrow i}^n$ and a tangential component $\mathbf{F}_{j \rightarrow i}^t$.

There are two different approaches to solving these equations of motion: the soft-sphere and the hard-sphere model. The soft-sphere model uses a global time step and performs time-integration over the sum of all forces acting upon the particles. Particles are allowed to overlap and contact forces are modeled, for example, using the Hertz-Mindlin model,

as illustrated in Fig. 2.1. These overlap-dependent force models take into account both single-particle mechanical properties such as the coefficient of restitution, the elasticity modulus and Poisson ratio, as well as frictional bulk properties. The maximum particle overlap should be kept under a value of 0.3% of the particle radius (Lommen et al., 2014) for numerical stability. This stability criterion restricts the global time step.

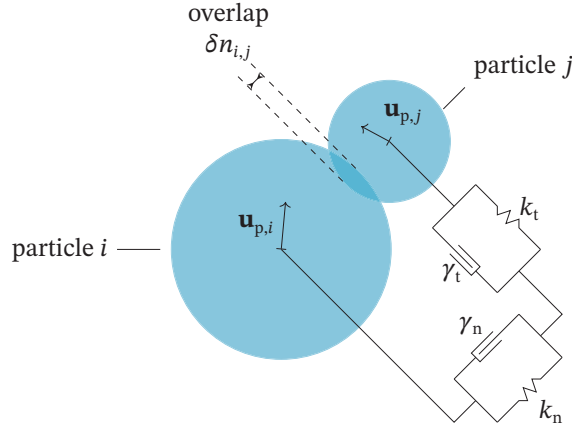


Fig. 2.1.: Schematic of particle overlap in the soft-sphere Discrete Element Method (DEM). Springs are indicated by the symbol for their coefficient k and dashpots are indicated by their viscous coefficient γ .

The hard-sphere model follows a localized approach to time stepping, where particle tracks are assumed to be linear or linearly accelerated/dampened until a collision is detected. Then, the coefficient of restitution is applied to the colliding elements, the deflection is applied to the velocity vectors and calculation resumes. The operation is periodically interrupted to recalculate non-contact forces.

While the effective timestep is much lower in soft-sphere models, hard-sphere models are rarely chosen for bulk solids due to the high incidence of particle contacts and a high collision frequency. As every collision requires an interruption of calculation, the hard-sphere model is rarely used for these cases.

In soft-sphere simulations, contact forces are calculated according to the Hertz law in the normal direction (Kloss et al., 2012):

$$\mathbf{F}_{j \rightarrow i}^n = k_n \delta \mathbf{n}_{ij} - \gamma_n \mathbf{u}_{p,i,j}^n \quad (2.3)$$

$$\mathbf{F}_{j \rightarrow i}^t = k_t \delta \mathbf{t}_{ij} - \gamma_t \mathbf{u}_{p,i,j}^t \quad (2.4)$$

where k is the elastic coefficient, $\delta \mathbf{n}_{ij}$ and $\delta \mathbf{t}_{ij}$ are the normal and tangential overlaps, γ is the damping coefficient and $\mathbf{u}_{p,ij}$ is the relative velocity.

These coefficients can be calculated from bulk solids parameters such as the particle mass m_i , the radius R_i , the modulus of elasticity Y_i and the coefficient of restitution e using the model equations given in Tab. 2.1.

Tab. 2.1.: Hertz-Mindlin-Tsuji contact model quantities.

Quantity	Expression
Spring stiffness	
Normal	$k_n = (4/3)Y^* \sqrt{r^* \delta n_{ij}}$
Tangential	$k_t = 8G^* \sqrt{r^* \delta n_{ij}}$
Damping coefficient	
Normal	$\gamma_n = -2\sqrt{5/6}\beta\sqrt{S_n m^*} \geq 0$
Tangential	$\gamma_t = -2\sqrt{5/6}\beta\sqrt{S_t m^*} \geq 0$
Stiffness	
Normal	$S_n = 2Y^* \sqrt{r^* \delta n_{ij}}$
Tangential	$S_t = 8G^* \sqrt{r^* \delta n_{ij}}$
Scaling parameter	$\beta = \ln(e)/\sqrt{\ln^2(e) + \pi^2}$
Effective quantities	
Young's modulus	$Y^* = 1/((1 - \nu_1^2)/Y_1 + (1 - \nu_2^2)/Y_2)$
Shear modulus	$G^* = 1/(2(2 - \nu_1)(1 + \nu_1)/Y_1 + 2(2 - \nu_2)(1 + \nu_2)/Y_2)$
Radius	$r^* = 1/(1/r_1 + 1/r_2)$
Mass	$M^* = 1/(1/M_1 + 1/M_2)$

Thus, both elastic compressibility and inelastic energy dissipation are contained. Frictional effects are included by enforcing the Coulomb criterion

$$F_{j \rightarrow i}^t \leq \mu_{fr} F_{j \rightarrow i}^n \quad (2.5)$$

that truncates the tangential force exerted to a value relative to the normal force acting, considering the static friction coefficient μ_{fr} .

The torque due to particle contact was considered using an elastic-plastic spring pot torque model as formulated by Ai et al. (2011) that adds an elastic (superscript k) and a dissipative (superscript d) term:

$$\mathbf{T}_{j \rightarrow i} = \mathbf{T}_{j \rightarrow i}^k + \mathbf{T}_{j \rightarrow i}^d \quad (2.6)$$

The elastic term is given by

$$\mathbf{T}_{j \rightarrow i}^k(t + \Delta t) = \mathbf{T}_{j \rightarrow i}^k(t) - k_{\text{rfr}} \Delta \theta \quad (2.7)$$

with k_{rfr} being the rolling stiffness and $\Delta \theta$ the *incremental* relative rotation between the particles in the shear plane. $\Delta \theta$ is limited using the coefficient of rolling friction, μ_{rfr} , relative to the normal contact force component:

$$T_{j \rightarrow i}^k \leq \mu_{\text{rfr}} r^* F_{j \rightarrow i}^n. \quad (2.8)$$

The rolling stiffness is related to the tangential stiffness k_t by

$$k_{\text{rfr}} = k_t (r^*)^2. \quad (2.9)$$

In the applied variant of the elastic spring-dash pot model, the viscous damping contribution is deactivated.

The computational demand of DEM simulation lies in both the size of the time step Δt , as well as the number of elements to be considered. General performance (number of time steps per unit time) can be increased by artificially softening particles, leading to longer collision times. Lommen et al. (2014) has shown that this simplification has little influence on macroscopic system behavior. This accelerates simulations, but does not allow the consideration of smaller particles or larger industrial systems containing more than tens of millions of particles.

2.2. Governing Equations in Computational Fluid Dynamics

Fluid flow in CFD-DEM coupling is usually resolved by applying the finite volume method to the Navier–Stokes equations to yield a velocity field \mathbf{u}_f and pressure field p that are discretized on a grid consisting of cells that constitute a number of interconnected control volumes:

$$\frac{\partial (\alpha_f \rho_f \mathbf{u}_f)}{\partial t} + \nabla \cdot \alpha_f \rho_f \mathbf{u}_f \mathbf{u}_f = -\alpha_f \nabla p + \alpha_f \nabla \cdot \boldsymbol{\tau} + \alpha_f \rho_f \mathbf{g} + \dot{\mathbf{S}}_u \quad (2.10)$$

$$\alpha_f \frac{\partial (\alpha_f \rho_f)}{\partial t} + \nabla \cdot \alpha_f \rho_f \mathbf{u}_f = 0. \quad (2.11)$$

Here, α_f denotes the volumetric phase fraction of the fluid phase, ρ_f its density, \mathbf{u}_f its real (interstitial) velocity, \mathbf{g} is the gravitational acceleration and $\dot{\mathbf{S}}_u$ is a momentum exchange term.

The pressure p is not directly solved for using the continuity equation (2.11) but is instead iterated using a pressure equation to enforce continuity. The shear stress tensor $\boldsymbol{\tau}$ is given using a Newtonian law of viscosity or a more sophisticated closure. A relation between density, pressure, velocity and other state variables (most notably the temperature T_f) is required for the compressible case. Usually, the ideal gas equation $\rho_f = p / (R_f T_f)$ is used, with R_f being the mass-specific gas constant.

This formulation of the Navier-Stokes equations, referred to in literature (e.g. by Zhou et al. (2010) and Zhu et al. (2008)) as model A, includes the fluid volume fraction α_f and the momentum exchange term $\dot{\mathbf{S}}_u$ that represent the presence of a Lagrangian phase, summarized in Tab. 2.2. The other formulation, model B, considers pressure to be attributed to the fluid phase, in contrast to model A, which assumes a shared pressure among both phases. Consequently, the pressure gradient term in model B reads $-\nabla p$, and the shear stress term $\nabla \cdot \boldsymbol{\tau}$. This also causes the phase interaction forces to be summed up over the total control cell volume V_{cell} in model A and the fluid volume $\alpha_f V_{\text{cell}}$ in model B, respectively.

Tab. 2.2.: Attributions of different momentum contributions in model A and model B formulations of CFD-DEM coupling.

Term	Model A	Model B
Shear stress	$\alpha_f \nabla \cdot \boldsymbol{\tau}$	$\nabla \cdot \boldsymbol{\tau}$
Pressure gradient	$\alpha_f \nabla p$	∇p
Momentum exchange control volume	V_{cell}	$\alpha_f V_{\text{cell}}$

The forces involved include at least

- the drag force,
- the pressure gradient force, and
- the viscous force.

In liquid-solid systems,

- the virtual mass force and
- Basset force

are required in addition to the aforementioned ones to accurately depict the effects of boundary layers (Nijssen et al., 2020).

When effects like particle rotation are to be considered,

- the Saffmann shear lift force and
- the Magnus force

contribute additional source terms that induce a torque into the fluid phase and have to be treated with further numerical effort. Although all of these forces may be present in any given physical system, their contribution might be negligible in modeling and selectively ignored to reduce computational demand.

2.2.1. Turbulence Modeling

Starting from a given flow velocity, a viscous fluid will exhibit highly non-linear, chaotic behavior due to energy dissipation in the form of vortices that form and break up on a wide range of length scales. Describing this behavior in simulations requires the spatial and temporal resolution of the range from very small length scales to large eddies in the system. Thus, the accurate representation of turbulent flows requires turbulence modeling for all practical intents and purposes. A rigorous treatment of these models can be found in the textbook by Wilcox (2006). For the fluid phase, turbulent viscosity/Reynolds-averaged Navier–Stokes models like the k - ε or k - ω models are used, which solve additional differential equations for the generation, transport, and dissipation of the turbulent kinetic energy and increase the viscosity depending on these quantities. As such, the effect of turbulence on averaged flow is captured without resolving the small length scales. Large eddy simulations, in which eddies larger than a filtering criterion are resolved, are performed less frequently. In these, the effect of those eddies occurring on smaller length scales is modeled using an isotropic model like k - ε . In both cases, the effect on particles can be stochastically modeled by using the time spent in an eddy and the turbulent velocity fluctuation, both of which depend on the turbulent kinetic energy.

2.3. Eulerian-Lagrangian Phase Coupling

As illustrated in Fig. 2.2, phase coupling is realized by introducing source-sink terms into the mass and momentum, as well as heat and species balances on the CFD side, as well as respective source-sink terms on the DEM side. The rate at which these are transferred between the phases is described using closures that normally take the fluid-mechanical and compositional situation into consideration. Algorithmically, the CFD and DEM part of the simulation are alternated, with coupling steps in between. In the coupling steps, the source-sink terms are recalculated based on the changed situation. Furthermore, mapping